lajss.org
Latin American Journal of Solids and Structures
www.lajss.org

The influence of stand-off distance on the penetration characteristics of Toroidal Explosively Formed Projectile (TEFP)

Weijian Tang[a] 0009-0005-8351-6196, Chong Ji[a] 0000-0003-3428-6302, Yuting Wang[a*] 0000-0001-9893-5610, Xin Wang[a] 0000-0002-9572-9288, Changxiao Zhao[a] 0000-0002-4545-4618, Huanyu Qian[a] 0009-0000-7112-5933

[a] College of Field Engineering, Army Engineering University of PLA, Nanjing 210007, China. E-mails:2454566100@qq.com; 2468645816@qq.com; wangyuting@njust.edu.cn; 310433804@qq.com; 360349734@qq.com; huanyu_qian@163.com

* Corresponding author.

Abstract

The penetration and reaming performance of a toroidal explosively formed projectile (TEFP) warhead with a charge diameter (D) of 56 mm was investigated when it was used to penetrate Q235 steel targets that were 10 mm thick at different stand-off distances (h). Thought the experimental and numerical result, the formation and penetration mechanisms of TEFP was revealed, and the differences between the radial and axial velocities in various portions of the TEFP were the primary causes of the TEFP expansion and rupture. When the TEFP tail has not completely ruptured and detached (h < 2.14D), TEFP has a strong penetration ability, resulting in TEFP perforating the target plate. The perforation process included three phases: pit opening, plastic hole expansion, and shear-block formation; these phases had average energy consumption ratios of 26.0%, 56.8%, and 17.2%, respectively. Finally, a method of evaluating the perforation and reaming capability of the TEFP was developed and used to identify the optimal stand-off distance, h_0 = 1.96D, which produced a penetration hole with a diameter of 1.875D.

Keywords

TEFP, Q235 steel plate, reaming, stand-off distance, penetration

Graphical Abstract

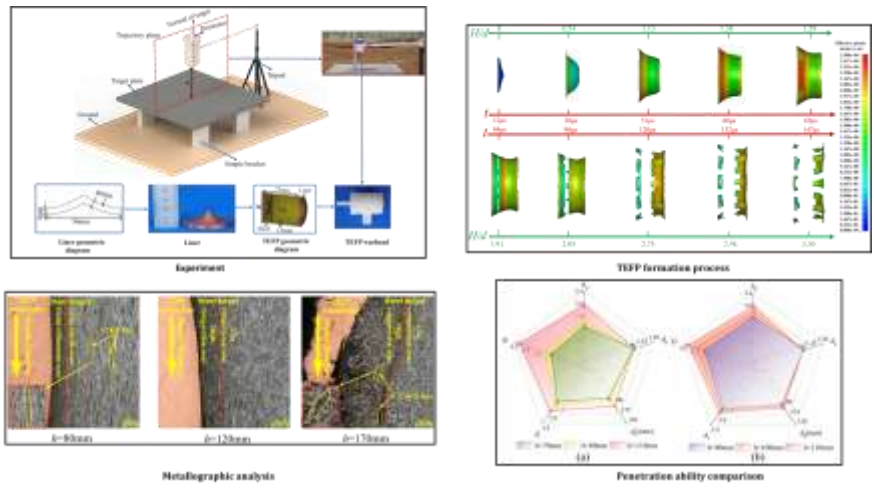

1. INTRODUCTION

Shaped charges have been extensively used in military and civilian applications, such as petroleum perforation, rapid hole-punching, and weapons development (2002, 2017, 2018). Shaped charges are commonly capable of forming one of three distinct penetrator types: shaped charge jets (SCJs), explosively formed projectiles (EFPs), and jetting projectile charges (JPCs). In recent years, many scholars have investigated the formation, penetration, and reaming capabilities of SCJs, EFPs, and JPCs.

Guo (2018) investigated the penetration of thick steel plates by a reactive-liner shaped charge jet (RLSCJ). Four stand-off distances—0.5*CD*, 1.0*CD*, 1.5*CD*, and 2.0*CD* (where *CD* refers to the charge diameter)—were selected for the penetration experiments. The experimental results showed that the RLSCJ produced a larger hole diameter but a smaller penetration depth than traditional metal-liner SCJs when used to penetrate a thick steel plate. At stand-off distances from 0.5*CD* to 1.5*CD*, the RLSCJ produced fragmentation effects. Dehestani (2019) investigated the effects of geometric parameters on the penetration performance of SCJs during their formation processes. It was found that increasing the stand-off distance increased the jet formation length, which could enhance the penetration depth of the jet. However, when the stand-off distance increased beyond a certain critical threshold, the maximum velocity of the SCJ decreased, thereby leading to fragmentation of the SCJ and a consequent reduction in the penetration capability of the jet. Wang (2018) investigated the effects of the liner material and cone angle on a shaped charge that was used to penetrate layered and spaced concrete targets. The results indicated that the shaped charge with a copper liner penetrated the concrete targets most deeply, while the charge with an aluminum liner produced the largest hole diameter.

Fu (2013) investigated the penetration performance of three JPC types at large stand-off distances. The results indicated that the rod-like jet formed by a spherical segmented liner had the best penetration performance at large stand-off distances; this jet produced a hole with a diameter equal to 50% of the charge diameter. Chen (2015) designed an eccentric semispherical liner, analyzed the influence of its structural parameters on the collision pressure of the detonation waves, and obtained expressions for the jet mass and velocity distributions by varying the thickness of the liner while holding the mass constant. A comparison of different thickness schemes enabled the jet mass to be increased by 29.5% and the head velocity to be increased by 21.3% when the liner was thick at the top and bottom but thin in the middle.

Liu (2017) investigated the dynamic responses of copper- and iron-lined EFPs used to impact finite steel targets at high velocities. It was found that the copper liner had a better penetration capability than the iron liner. Cardoso and Teixeira-Dias (2016) proposed a numerical model to predict the effects of the liner material and thickness, the explosive type, and the number of detonators on the formation and ballistic capabilities of EFPs. Han (2019) investigated the formation and penetration processes of Zr–Ta liners with various inner–outer liner thickness ratios. The results showed that, for a constant charge and a constant stand-off distance, a smaller thickness ratio corresponded to slower EFP formation, a weaker penetration capability, and a stronger reaming capability.

The diversification of combat modes, as well as specific situations, such as the imminency of the following charge in a tandem warhead and the fast establishment of a rapid rescue channel, necessitate the formation of large-diameter holes in the targets. Because the average penetration-hole diameter produced by the shaped charges discussed previously is equal to 30–70% of the charge diameter, it is difficult to achieve these large-diameter requirements. To enhance the reaming capability of a warhead and thereby meet these requirements, it is necessary to explore warhead structures that can form holes with larger diameters. Therefore, many researchers have investigated shaped charge technologies that can create large-diameter holes in the targets. König and Mostert (2001) designed a shaped charge that could form an annular EFP. Their results showed that the diameter of the annular EFP formed by this structure was approximately equal to the charge diameter; meanwhile, the length of the EFP was approximately 33.3% of the charge diameter. Chick (1998) refined the annular shaped-charge structure by optimizing the thickness and cross-sectional shape of the liner, and thereby achieved a stable annular jet. This refined structure could form a penetration hole with a diameter equal to 75% of the charge diameter when the stand-off distance was 300% of the charge diameter. Xu (2019) proposed and validated a novel design for a bore-center annular shaped charge (BCASC) and investigated its performance when it was used to penetrate target plates. The results indicated that the location of the maximum wall thickness (θ) of the liner had the greatest influence on the radial and axial velocities of the projectile. As θ increased, the diameter of the penetration hole decreased and the penetration depth gradually increased. When θ = 30°, the target plate was penetrated with a hole that had a diameter equal to 92% of the charge diameter. Xu (2019) investigated the effects of three liner materials—molybdenum, nickel, and copper—on the formation and penetration characteristics of BCASCs when they were used to impact steel targets. The results indicate that, for a constant stand-off distance, the diameters of the penetration holes created by the three liner materials all exceeded the charge diameter, and that the molybdenum liner produced the deepest penetration. Meister and Haller (2001) designed a novel annular shaped-charge structure

and investigated its penetration capabilities. The results indicated that this shaped-charge structure, when used with a variety of liner materials, such as iron, aluminum, lead, and tantalum, was capable of forming stable annular EFPs at a specific stand-off distance. Moreover, the iron liner was able to produce a penetration hole in a steel target with a diameter equal to 127% of the charge diameter and a depth equal to 38% of the charge diameter.

The annular shaped charge discussed above has significantly enhanced the penetration-hole diameter with respect to those produced by traditional shaped charges. However, the penetration-hole diameter is still limited to sizes that are insufficient for the requirements discussed previously. Richard (2010) designed a novel shaped-charge structure that, upon detonation, produced a toroidal explosively formed projectile (TEFP). Experimental validation showed that the TEFP warhead could create an opening in a reinforced concrete wall with a diameter equal to 210% of the charge diameter and TEFP could cut the rebar framework to form a hole with a diameter equal to the charge diameter. However, the formation and penetration processes of the TEFP remain unclear, and the mechanisms by which the key factors affect the penetration behavior require clarification. During this study, by referencing the shaped-charge structures reported in the literature, a TEFP warhead with a charge diameter of 56 mm was designed and penetration tests were conducted with Q235 steel targets. A numerical simulation model for the formation and penetration processes of the TEFP was developed and used to analyze the effects of the TEFP on these processes. It was also used to investigate the impacts of the stand-off distance on the macroscopic and microscopic penetration characteristics in the target plate. A method of assessing the penetration and reaming capabilities of this TEFP structure was also developed.

2. Experimental Setup

Figure 1 presents a schematic diagram of the experimental setup used to investigate the penetration of Q235 steel targets by the TEFP warhead. The experimental setup included the TEFP warhead, a target plate, a simple bracket, and a tripod used to adjust the stand-off distance (*h*) of the TEFP warhead. The target plate had dimensions of 500 × 500 × 10 mm, and it was supported by a simple bracket at its base. The TEFP warhead was vertically aligned with the target plate using a tripod stand. The knob on the left side of the tripod stand was used to adjust the *h* of the TEFP warhead. The detonation point of the warhead was located at the bottom center of the charge.

The TEFP warhead was composed of a liner, an explosive, and a plastic shell. The shell was composed of plastic resin and had a wall thickness of 1.5 mm. The liner was composed of oxygen-free copper and featured an equal wall thickness structure. It had a bottom diameter (*D*) of 56 mm, a curvature radius of 60 mm, and a wall thickness of 4 mm. The TEFP utilized a C4 plastic explosive, which had a density of 1.304 g/cm^3, a charge diameter of 56 mm, and a height of 73 mm. To investigate the penetration characteristics of the TEFP warhead on the target plate at different values of *h*, penetration experiments were conducted with four different *h* values: 80 mm, 120 mm, 170 mm, and 230 mm.

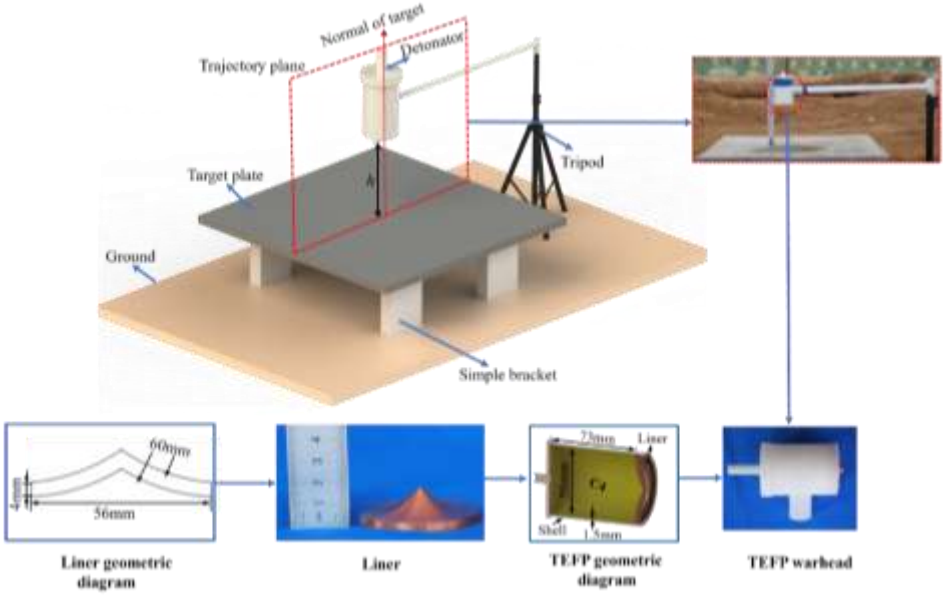

Figure 1 *Schematic diagram of the experimental setup used to test the TEFP warhead*

3. Experimental Results

Figure 2 presents the penetration results when the TEFP warhead was used to penetrate Q235 steel plates at different *h* values. When *h* = 80 mm, the TEFP completely perforated the target plate, but complete perforation did not occur for the other *h* values. When *h* = 120 mm, a distinct circular bulge and local cracks were observed on the back side of the target plate, and the target plate was critically perforated. When *h* = 170 mm, spalling in the target plate resulted in localized perforation and the detachment of certain zones on the back side. When *h* = 230 mm, the target plate exhibited discontinuous annular bulging on its back side. As *h* increased, the penetration-hole diameter also increased, and the shape of the penetration hole on the front side of the target plate transitioned from a continuous annular shape to a discontinuous annular shape. At different *h* values, copper adhered to the penetration channels in the target plates, and the front sides of the target plates had zones with varying degrees of fragment damage. The fragment damage zones increased in size as *h* increased, while the damage density decreased. Observations of the sides of the target plates revealed that, except for when *h* = 170 mm, flanging occurred on the target plates, and that the degree of flanging decreased as *h* increased.

The copper adhesion within the penetration channels at different *h* values occurred because the steel plates were subjected to high temperatures, high pressures, and high strain rates during the high-velocity TEFP impacts. These extreme conditions caused some of the copper to melt. In addition, oxygen-free copper exhibits a certain degree of adhesiveness under high-temperature and high-pressure conditions; this adhesiveness caused the copper to adhere to the penetration channels in the target plates. The primary reasons for the appearance of fragment damage zones on the front sides of the target plates and the differences in the TEFP penetration capabilities at different *h* values are discussed next. The effects of the detonation wave and the detonation products caused some of the TEFP material to undergo fragmentation. The resulting fragments eventually penetrated the target plate, thereby leading to the formation of fragment damage zones. The fragments possessed certain radial velocities and velocity gradients; these led to increases in the size of the fragment damage zone but decreases in the density as *h* increased. Moreover, the shapes of the penetration holes on the front sides of the target plates indicated that the TEFP maintained an optimal formation at lower *h* values, but that as *h* increased, the TEFP began to rupture. This rupture was the primary cause of the decline in the penetration capability of the TEFP.

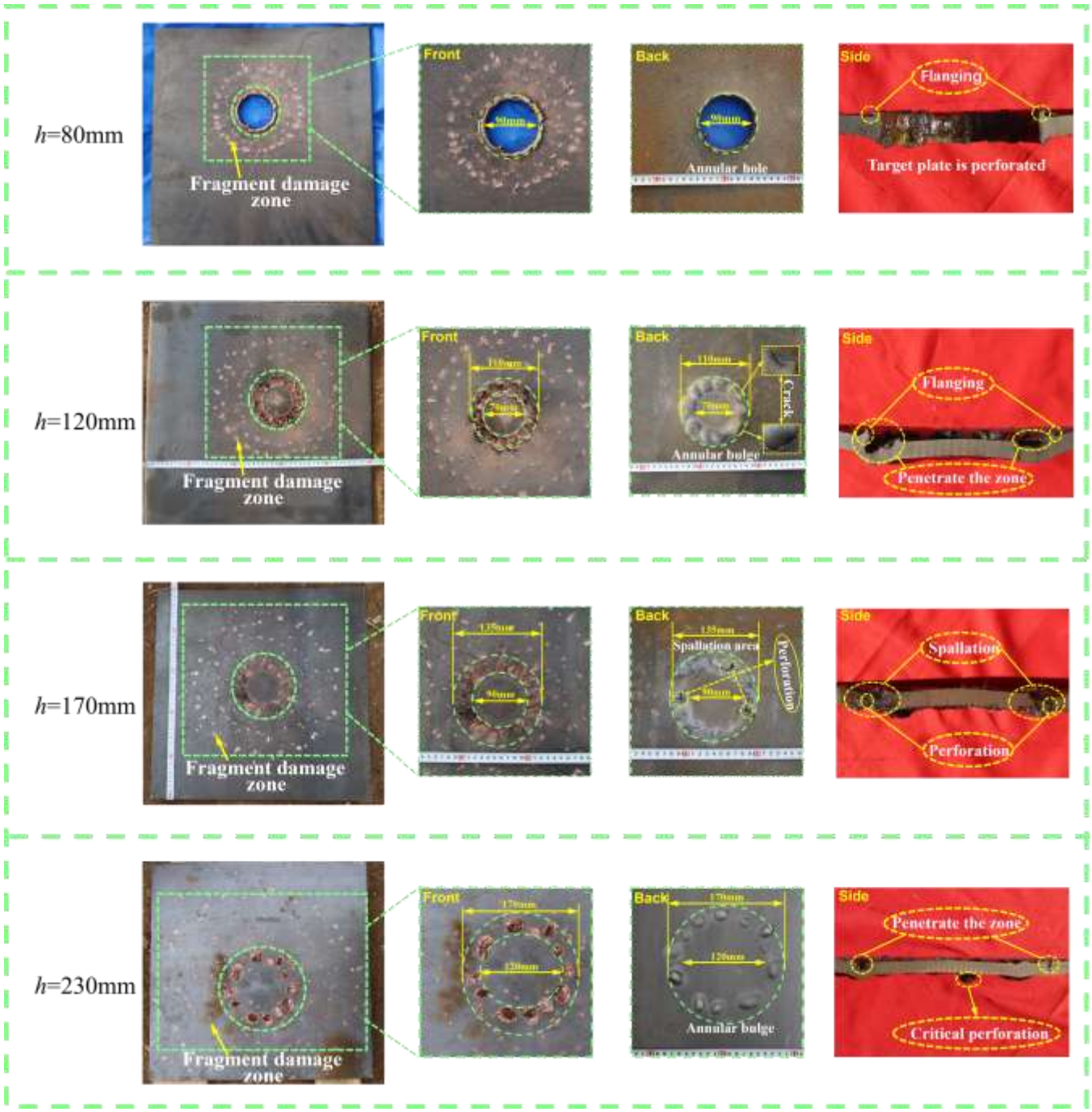

Figure 2 *Characteristics of the Q235 steel plate damage for different h values*

The penetration-hole zones were also investigated for three typical stand-off distances (80, 120, and 170 mm) using a microstructural analysis. Figure 3 presents microstructural micrographs of the target plates for these three stand-off distances. The figure shows that the microstructures of the target plates possessed two distinct states with a clear boundary line at the different *h* values. The degree of compression of the target plate material near the wall of the penetration hole (on the left side of the boundary line) was significantly greater than that further from the wall of the penetration hole (on the right side of the boundary line). Furthermore, copper adherence was observed on the penetration-hole wall (on the left side of the boundary line).

When *h* = 80 mm, the target plate exhibited micro-cracks that were non-uniformly distributed. Additionally, the compression in the region near the wall of the penetration hole (on the left side of the boundary line) was greater than that for other values of *h*. In the region further from the wall of the penetration hole (on the right side of the boundary line), the grains had markedly elongated in the direction of the impact loading. When *h* = 170 mm, the target plate exhibited very distinct micro-cracks. When *h* = 120 mm, no distinct micro-cracks could be seen on the target plate.

However, the region further from the penetration-hole wall experienced slight elongation with respect to the same region when *h* = 170 mm.

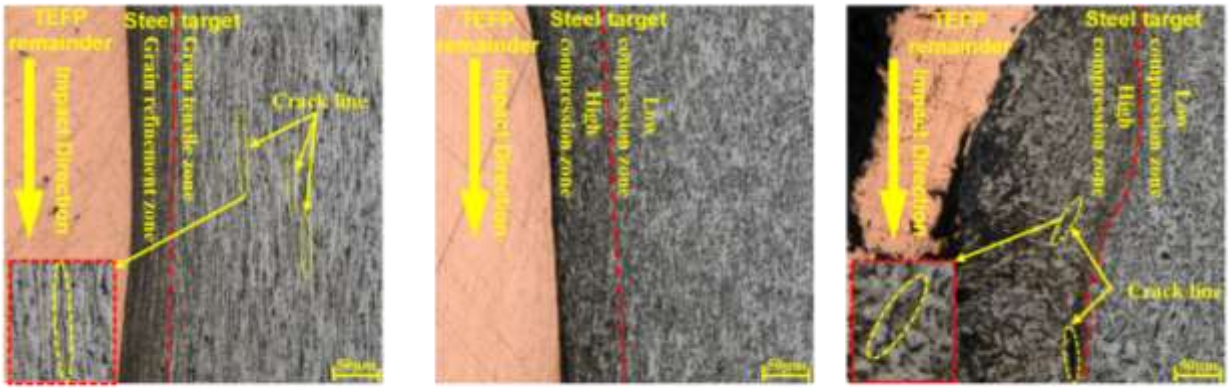

Figure 3 *Metallographic micrographs of the target plates for three typical stand-off distances*

According to the theory proposed by Murr (2002), the micro-dynamic evolution process of metal grains subjected to a strong load involves crushing, elongation, refinement, and recrystallization. Therefore, it was inferred that, when *h* = 80 mm, the grains of the steel plate were subjected to a strong impact that led to significant grain refinement and recrystallization near the wall of the penetration hole (on the left side of the boundary line). When *h* = 120 mm and *h* = 170 mm, however, the grains of the steel plates were subjected to relatively minor impacts and they did not progress to the refinement and recrystallization stages. These results are consistent with the macroscopic damage that was observed on the steel plates impacted by the TEFP at different *h* values, and they further indicate that, as *h* increased, the TEFP rupture caused penetration-capability reductions.

4. Numerical Simulation of the TEFP Penetration into Q235 Steel Targets

4.1 Development of the simulation model

To more accurately study and analyze the various changes in the TEFP formation and penetration processes, as well as to reveal the mechanisms behind these processes, a numerical simulation model for TEFP formation and penetration of Q235 steel targets was established in the LS-DYNA finite element software. The finite element model of the TEFP warhead is shown in Figure 4. To simplify the calculations, a three-dimensional finite element model that included 1/4 of the total structure was constructed, and symmetric boundary conditions were applied to the symmetry planes of the 1/4 model. To improve the efficiency of the calculations, the support effect of the simple bracket was achieved in the computational model by the application of boundary constraints to the target plate. All the models used Lagrangian grids and multi-faceted solid elements (SOLID164) with eight nodes. The "*CONTACT_SLIDING_ONLY_PENALTY" keyword was used to simulate the contact between the explosive and the liner. The "*CONTACT_ERODING_SURFACE_TO_SURFACE" keyword was used to simulate the contact between the TEFP and the target plate. Many numerical calculation results have shown that the interactions between a detonation product and the corresponding liner had little effect 28 μs after the detonation of the explosive (Li 2009). Therefore, the "*MAT_ADD_EROSION" keyword was added to the simulation model in this study to remove the explosive.

The HyperMesh software was used to generate the grids for the simulation model. The target plate was subdivided in the regions that were in contact with the TEFP. Figure 4(c) depicts the grid divisions of the Q235 steel plate, for which the cell dimensions in zone 1 were 1 × 1 × 1 mm. The cell dimensions in zone 2 were 2 × 1 × 1 mm, and the cell dimensions outside of zones 1 and 2 were 2 × 2 × 1 mm. The numerical calculations were performed in the LS-DYNA software, and the length, mass, and time units used were cm, g, and μs, respectively. The entire process of TEFP penetration into a Q235 steel target was simulated for the experimental stand-off distances, as well as for four additional stand-off distances (70, 90, 100, and 110 mm). The simulations assumed that the explosive, plastic shell, liner, and Q235 target plate were all composed of homogeneous, continuous media, and that the entire explosive penetration process was adiabatic and was not influenced by gravity. The side effects of the target plate were ignored, as well as the overall motion of the target plate and the influence of air.

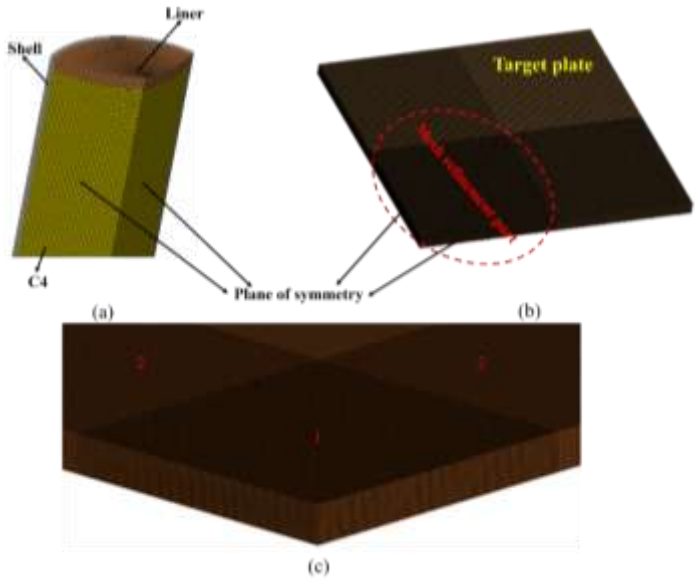

Figure 4 *Finite element model: (a) TEFP warhead, (b) Q235 target plate, (c) subdivided grid regions of the target plate.*

4.2 Material constitutive model and parameters

In this study, the charge was simulated using the LS-DYNA numerical calculation software. The charge contained in the TEFP warhead was described by a constitutive model for high explosives, "*MAT_HIGH_EXPLOSIVE_BURN". The Jones–Wilkins–Lee (JWL) equation of state was used in this constitutive model, and it is presented here as Equation (1):

$$P = A(1-\frac{\omega}{R_1 V})e^{-R_1 V} + B(1-\frac{\omega}{R_2 V})e^{-R_2 V} + \frac{\omega E}{V} \tag{1}$$

Where ρ is the density, P represents the detonation pressure, E is the internal energy per unit volume, and V is the relative volume. A, R_1, B, R_2, and ω are material constants. In this paper, the density of C4 explosive in the experiment is 1.304 g/cm^3 . During the numerical simulation process, according to the method proposed by Shen Fei (Shen Fei 2014), theoretical corrections were made based on the material parameters of C4 explosive with a density of 1.601 g/cm^3 in the literature published by R Qi (R Qi 2020). The material parameters of C4 explosive after theoretical correction are shown in Table 1.

Table 1 Explosive parameters

ρ/(g·cm^{-3})	D/(cm·μs^{-1})	A/GPa	B/GPa	R_1	R_2	P_{CJ}/GPa
1.304	0.6505	337.17	9.0368	4.9	1.3	13.793

To accurately describe the dynamic response of the liner to an explosion impact, the circumferential impact of the detonation wave on the extrusion of the plastic shell and the failure modes at high temperatures, pressures, strains, and strain rates during the high-speed impact were examined. In this study, the Johnson–Cook (J–C) material model and the Gruneisen equation of state were used to describe the formation and penetration processes of the TEFP. The expression for the yield stress of the material used in the J–C model is provided in Equation (2):

$$\sigma_y = (A_1 + B_1(\bar{\varepsilon}^P)^n)\left(1 + C\ln\dot{\varepsilon}^*\right)(1-(T^*)^m) \tag{2}$$

Where A_1, B_1, C, n and m are the material parameters determined by experiments. $\bar{\varepsilon}^p$ is the equivalent plastic strain, $\dot{\varepsilon}^* = \dot{\varepsilon}_p / \dot{\varepsilon}_0$ is the dimensionless effective strain rate at a reference strain rate $\dot{\varepsilon}_0 = 1s^{-1}$. T^* is the homologous temperature which is defined by $T^* = (T-T_{room})/(T_{melt}-T_{room})$, where T is the current temperature, T_{room} and T_{melt} are the room and melting temperatures, respectively.

Johnson and Cook also developed a failure criterion that accounts for temperature, strain rate and strain path in addition to the triaxiality of the stress state. The model is based on damage accumulation, and has the basic form:

$$D = \sum \frac{\Delta \varepsilon_y}{\varepsilon_f} \tag{3}$$

Where D is the damage to a material element, $\Delta\varepsilon_y$ is the increment of accumulated plastic strain, and ε_f is the accumulated plastic strain to failure under the current conditions of stress triaxiality, strain rate and temperature. Failure occurs when D=1, and in the finite element simulations, element erosion is used to remove elements that have reached the critical damage. The failure strain ε_f is defined as:

$$\varepsilon_f = \left[D_1 + D_2 \exp D_3 \sigma^* \right] \left[1 + D_4 \ln \dot{\varepsilon}^* \right] \left[1 + D_5 T^* \right] \tag{4}$$

Where σ^* is the dimensionless pressure-stress ratio defined as $\sigma^* = \sigma_m / \bar{\sigma}$ is the mean stress normalized by the effective stress, $\bar{\sigma}$ is the effective stress, and D_1, D_2, D_3, D_4 and D_5 are the material parameters. The material parameters and equations of state involved in the numerical calculation are shown in Tables 2 and 3. The value ranges of the material parameters were selected based on previous publications (Gao Y X 2024,Johnson G R 1985,Mengtao Zhang 2023).

Table 2 Main parameter values for the Johnson-Cook material model

materials	ρ/(g/cm^3)	G/(GPa)	A_1/(GPa)	B_1/(GPa)	C	n	m
oxygen-free copper	8.96	46	0.9E-3	2.92E-3	0.025	0.31	1.09
Q235 steel plate	7.8	75	0.2938	0.2302	0.0652	0.578	0.706
materials	T_m/(K)	T_r/(K)	D_1	D_2	D_3	D_4	D_5
oxygen-free copper	1356	294	0.54	4.89	-3.03	0.014	1.12
Q235 steel plate	1795	300	0.472	18.728	-7.805	-0.0193	3.811

Table 3 Parameters of the Gruneisen equation of state

materials	C_1	S_1	S_2	S_3	γ_0	α
oxygen-free copper	0.394	1.489	0	0	2.02	0.47
Q235 steel plate	0.457	1.49	0.6	0	2.17	0

4.3 Comparison of the experimental and numerical simulation results

Figure 5 displays a comparison of the simulated and experimental penetration-hole shapes on the front and back sides of Q235 steel targets penetrated by the TEFP at different h values, demonstrating that the simulated penetration-hole shapes on both the front and back sides of the target plates were similar to the experimental shapes at various h values. Figure 6(a) presents a comparison of the simulated and experimental inner and outer penetration-hole diameters for different h values. The maximum error for the outer diameter was 3.6%, while that for the inner diameter was 14.2%. Figure 6(b) shows the comparison between the side shapes of the penetration-holes and the relevant penetration-hole sizes in the experiment and numerical simulation after the target plate is perforated (h=80mm). It can be seen that after the target plate is perforated, the degree of target plate flanging and the shape of the penetration hole are similar. Except for the relatively large error in the flanging length at the entrance of the target plate, the maximum error of the other penetration-hole sizes is 11.3%. Therefore, the numerical simulation model developed during this study effectively reflected the formation and penetration processes of the TEFP, and it was therefore suitable for further extended analyses.

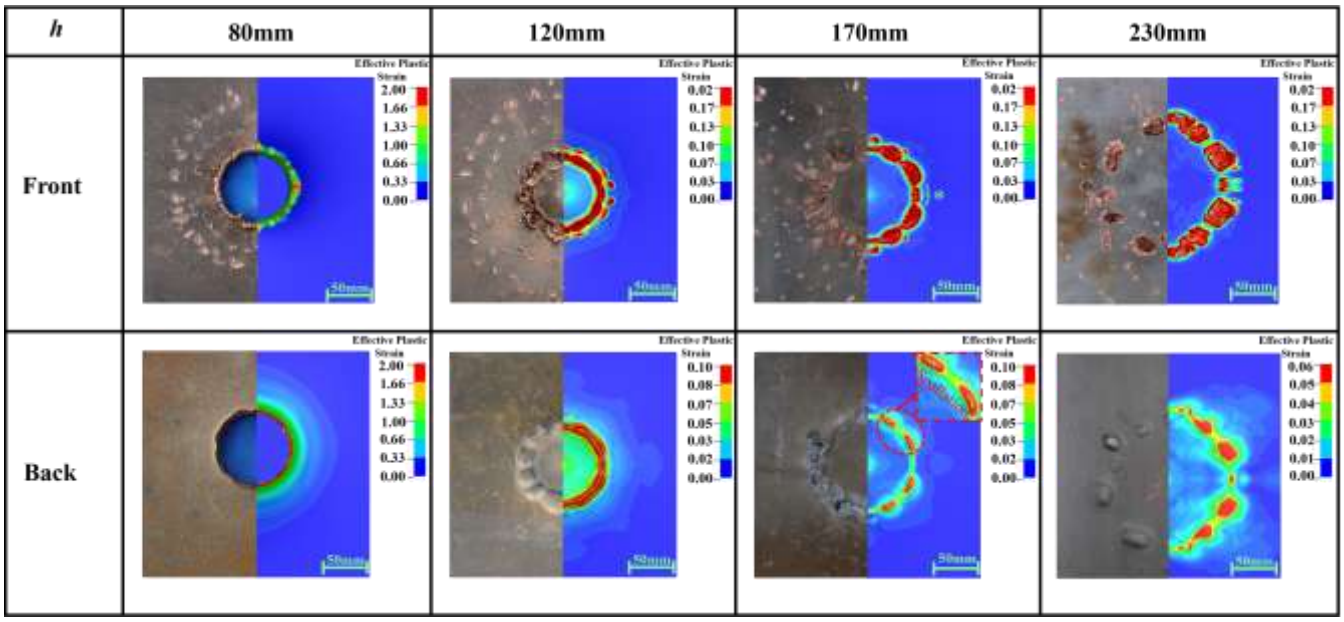

Figure 5 *Comparison of the experimental and simulated penetration-hole shapes*

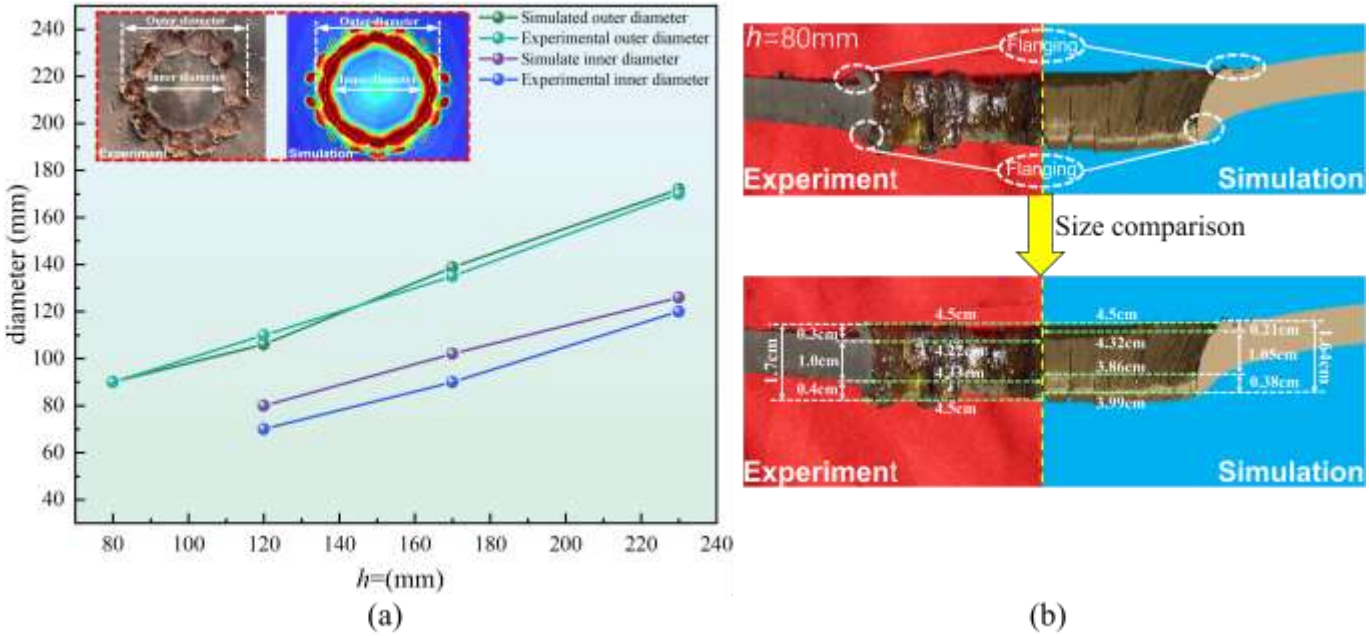

Figure 6 *Comparison of the experimental and simulated*: *(a) comparison of penetration-hole diameters (b) comparison of the side shapes and size of the perforation-hole after the target plate is perforated*

5. Effects of the TEFP Formation Process and the Stand-off Distance on the Penetration Characteristics

5.1 TEFP formation process

This study was conducted with the cross-section of the TEFP charge while considering the rotational symmetry of the charge structure. Assuming that the explosive charge detonates instantaneously, the detonation-driven effects of the explosive on the liner elements were divided into axial and radial components. The axial detonation-driven effect of the charge on a liner element can be described by the flat-plate ejection formula (Kenndey 1972, Wang 2017), while the radial detonation-driven effect can be described by the cylindrical crushing formula (Chou 1986). The velocity of a liner element, which is caused by the detonation-driven effects of the charge in both the axial and radial directions, can be obtained through the construction of a functional relationship. Then, the final velocity can be acquired. A schematic of the liner when it is subjected to axial and radial charge effects is depicted in Figure 7(a). In the schematic, *O* represents the center of the liner curvature, M_A is the mass of the liner element, M_a is the mass of the axial component of the charge

that corresponds to the liner element, M_r is the mass of the radial component of the charge that corresponds to the liner element, and M_s denotes the mass of the axial shell element that corresponds to the liner element. V_A, V_X, and V_Y represent the final velocity, the axial velocity component, and the radial velocity component of the liner element, respectively, θ is the angle between the liner element and the charge boundary axis, and α is the ejection angle of the liner element.

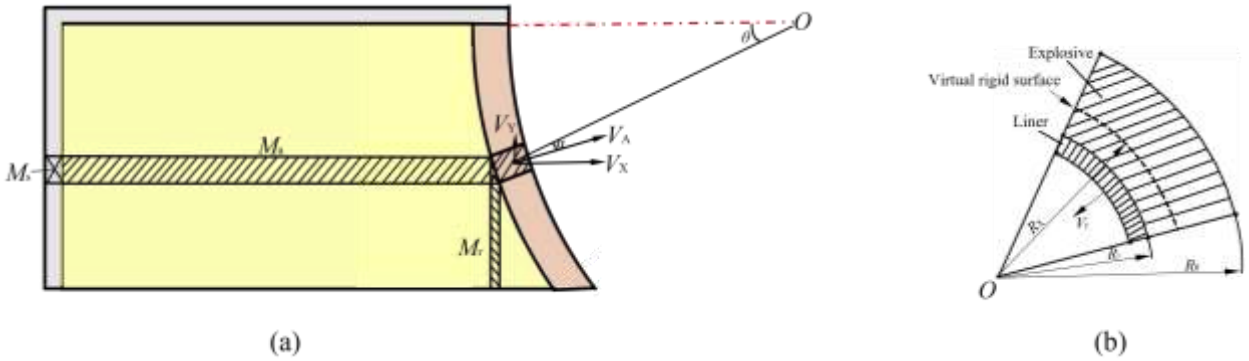

Figure 7 *Schematics of the charge effects on the liner: (a) effects of the explosive on a liner element (b) diagram of the cylinder implosion control body*

The velocity component V_a of the liner element produced by the axial component of the charge was derived from the flat-plate ejection formula. It is presented as Equation (5):

$$V_a = \sqrt{2E}\left[\frac{M_A}{M_a} + A^2\frac{M_s}{M_a} + \frac{1}{3}\frac{1+A^3}{1+A}\right]^{-\frac{1}{2}} \tag{5}$$

In Equation (4), $\sqrt{2E}$ is the Gurney constant for the explosive and A can be expressed by Equation (6):

$$A = \frac{2M_A + M_a}{2M_s + M_a} \tag{6}$$

The velocity component V_r of the liner element produced by the radial component of the charge was derived from the cylindrical crushing formula. It is presented as Equation (7):

$$V_r = \sqrt{2E}\left[\left(\frac{R_0^2 - R_i^2}{R_x^2 - R_i^2}\right)\frac{M_A}{M_r} + \frac{1}{6}\right]^{-\frac{1}{2}} \tag{7}$$

where R_0 and R_i represent the outer and inner diameters, respectively, of the radial explosive element and R_x is the radius of the virtual rigid surface inside the explosive (see Figure 7(b)).

The magnitude of V_A can be obtained by this method of dividing the explosive, as shown in Equation (8):

$$V_A = f(\theta)V_a + g(\theta)V_r \tag{8}$$

In Equation (7), $f(\theta)$ and $g(\theta)$ are continuous functions with respect to θ that satisfy the relationship in Equation (9):

$$f(\theta) + g(\theta) = 1 \tag{9}$$

Using a formula from the literature (Chou 1986), which indicates that $g(\theta) = \sin\theta$ can be substituted into Equation (8), Equation (10) was obtained:

$$V_{\mathrm{A}} = (1 - \sin\theta)V_{\mathrm{a}} + V_{\mathrm{r}}\sin\theta\,. \tag{10}$$

By substituting the expressions derived from Equations (5) and (7) into Equation (10), an expression for V_A was obtained. Then, the ejection angle can be calculated using Taylor's formula:

$$\alpha = \frac{V_{\mathrm{A}}\cos\varphi}{2U_{\mathrm{D}}} \tag{11}$$

In Equation (11), U_D represents the detonation velocity of the explosive and φ is the angle between the front vector of the detonation wave and the line that is tangent to the liner element.

V_X and V_Y can be expressed according to their geometric relationships by Equation (12):

$$\begin{cases} V_{\mathrm{X}} = V_{\mathrm{A}}\cos(\theta - \alpha) \\ V_{\mathrm{Y}} = V_{\mathrm{A}}\sin(\theta - \alpha) \end{cases}. \tag{12}$$

From equation (12), it can be seen that V_X and V_Y are related to V_A, θ, and α. θ changes with the location of the liner element, and α is related to the angle at which the detonation wave front reaches the liner, and the action angles of the detonation wave front at different locations of the liner are different, thus α and θ change according to the specific location of the liner element in the liner. From equations (5), (7), and (10), it is evident that V_A is related to M_a and M_r. The M_a and M_r values for the liner elements at different locations are different, which results in different velocities of the liner elements at different locations. Therefore, according to equation (12), due to the different values of V_A, θ, and α at different locations of the liner, the axial and radial velocities of the liner elements at different locations are also different.The magnitude of the axial velocity of the liner element (which propels the liner element forward along the charge axis) predominantly influences the penetration depth of the TEFP, while the radial velocity of the liner element (which propels the liner element outward along the charge radius) predominantly influences the penetration-hole diameter of the TEFP. The theoretical analysis discussed above indicates that different liner elements have different V_X and V_Y values; these velocity differences lead to stretching and rupture of the TEFP during its formation and penetration processes.

After detonation was initiated at the center of the explosive, a spherical detonation wave stably propagated through the charge. It first reached the shell, which then fragmented under the combined action of the detonation products and the shock wave. Figure 8 depicts the simulated strain and morphological evolution of the TEFP at different moments; in the figure, the ratio *H/d* is defined as the ratio of the flight distance to the base liner diameter of the TEFP. The detonation wave reached the liner at t = 12 μs. In the 12–28 μs range, the various impact forces that acted on different parts of the liner produced different radial and axial velocities in different parts of the TEFP. The shock wave and detonation products led to fragmentation of the TEFP head, and thus the formation of an opening. In the 28–69 μs range, the TEFP possessed a certain radial velocity and various axial velocities in different locations, which caused it to increase in both length and diameter as it traveled. The TEFP did not rupture, however, but exhibited a well-formed structure. In the 69–90 μs range, the TEFP tail gradually began to rupture, and at t = 90 μs, the tail had completely ruptured and detached. In the 90–147 μs range, axial rupture initiated in the residual portions of the TEFP, which ultimately resulted in the formation of radially distributed fragments.

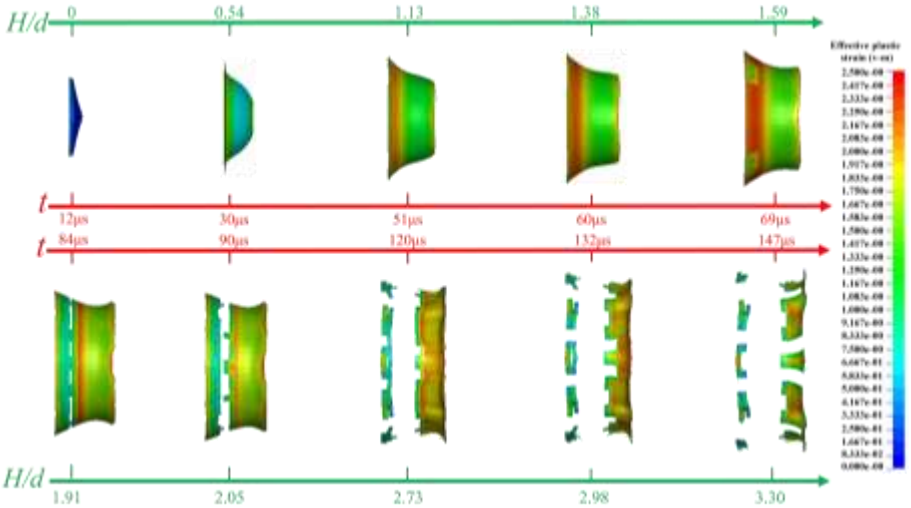

Figure 8 *TEFP morphological evolution and strain variations*

Using the results of the analysis discussed above, the TEFP formation process was divided into three distinct phases. The first phase was the opening phase of the TEFP (0–28 μs). During this phase, the effects of the shock wave and detonation products formed an opening in the TEFP head; in addition, the TEFP velocity reached its maximum value during this phase. The second phase was the stable expansion phase of the TEFP (28–69 μs). During this phase, the significant differences in the axial and radial velocities in different portions of the TEFP resulted in gradual increases in the TEFP length and diameter. The TEFP did not rupture during this phase, however, but exhibited a well-formed structure. At the end of this phase (t = 69 μs), the TEFP head had a diameter of 1.35*D*, a flight distance of 1.59*D*, and axial and radial velocities of 1370.8 m/s and 528.8 m/s, respectively. The third phase was the rupture and fragmentation phase of the TEFP (after 69 μs). During this phase, the strain in the TEFP tail first reached the limit of the material, thereby causing the tail to rupture and detach from the TEFP. Subsequently, the residual portions of the TEFP began to rupture, eventually forming radially distributed fragments.

Figure 9 depicts the variations in the axial and radial velocities, as well as in the diameters, of the TEFP head, middle, and tail throughout the three formation phases, showing that the radial velocity of the TEFP head was consistently greater than the velocities of the middle and tail. Additionally, the deformation energy that dissipated due to the radial expansion led to gradual decreases in the radial velocity of the TEFP after the opening phase. The TEFP diameter continuously increased throughout the formation process because of the inherent radial velocity of the TEFP. The TEFP head had the smallest diameter and the tail had the largest diameter during the opening and stable expansion phases. During the rupture and fragmentation phase, the head diameter gradually surpassed the middle and tail diameters. The axial velocity of the TEFP reached its maximum value at the end of the opening phase (t = 28 μs), and the axial velocity of the TEFP head was higher than the axial velocities of the middle and tail. After this, the axial velocity of the TEFP head gradually decreased while the axial velocities of the middle and tail increased. During the rupture and fragmentation phase, the axial velocities of the TEFP middle and tail gradually surpassed that of the head. Given that the axial velocity of the TEFP head was consistently higher than that of the tail prior to the rupture and fragmentation phase, the excessive difference between the axial displacements of the head and tail during this phase caused the TEFP tail to rupture and detach. The primary causes of the gradual decreases in the axial velocity of the TEFP head and the corresponding increases in the axial velocities of the middle and tail after the opening phase are discussed next. The radial velocity of the TEFP head was greater than the radial velocities of the middle and tail; these differences caused the head to exert a force on the middle and tail in the direction of the TEFP motion. Conversely, the middle and tail exerted a reaction force on the head, which resulted in increases in the axial velocities of the middle and tail and corresponding decreases in the axial velocity of the head.

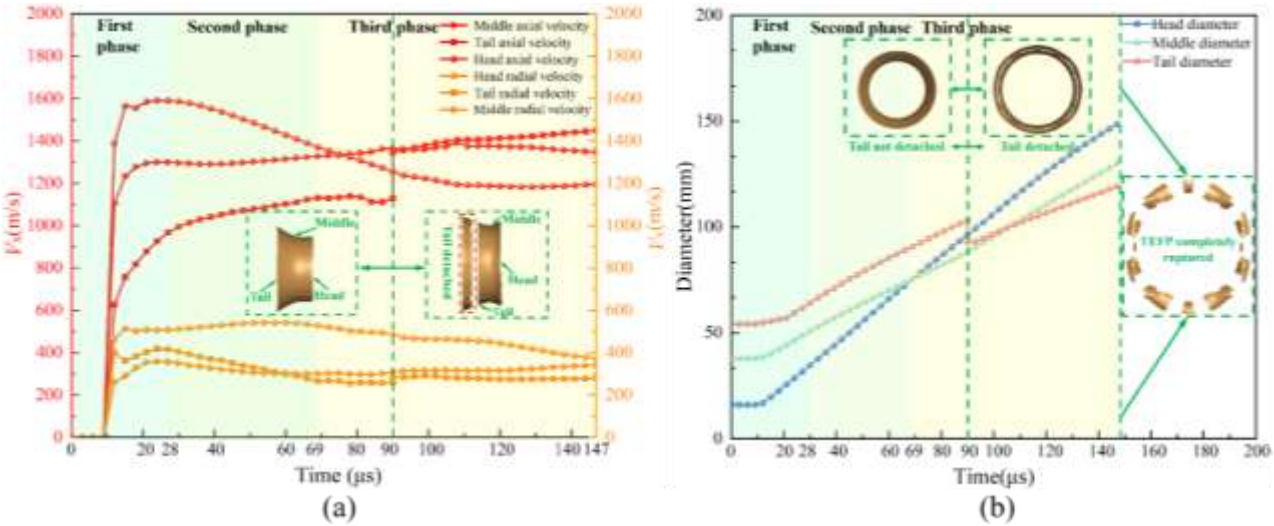

Figure 9 *TEFP characteristics during the formation process: (a) axial and radial velocities of the TEFP head, middle, and tail (b) diameters of the TEFP head, middle, and tail*

Figure 10 depicts the variations in the total energy, the kinetic energy, and the internal energy of the TEFP throughout its motion. The total and kinetic energies of the TEFP both increased sharply during the opening phase; they reached their maximum values of 86.376 and 81.280 kJ, respectively, at the end of this phase (t = 28 μs). During the stable expansion phase, the total and kinetic energies gradually decreased. From the beginning of the rupture and fragmentation phase to the formation of radially distributed fragments, sharp declines occurred in the total and kinetic energies of the TEFP. The internal energy variations of the TEFP took a parabolic form. The internal energy initially increased slowly and then decreased slowly, and it reached its maximum value of 7972 J at the end of the stable expansion phase (t = 69 μs). During the stable expansion phase, the total energy and kinetic energy of the TEFP decreased by 4.7 and 8.5%, respectively, from their maximum values. From the beginning of the rupture and fragmentation phase to the formation of radially distributed fragments, the total energy and kinetic energy decreased by 53.3 and 51.6%, respectively, from their maximum values.

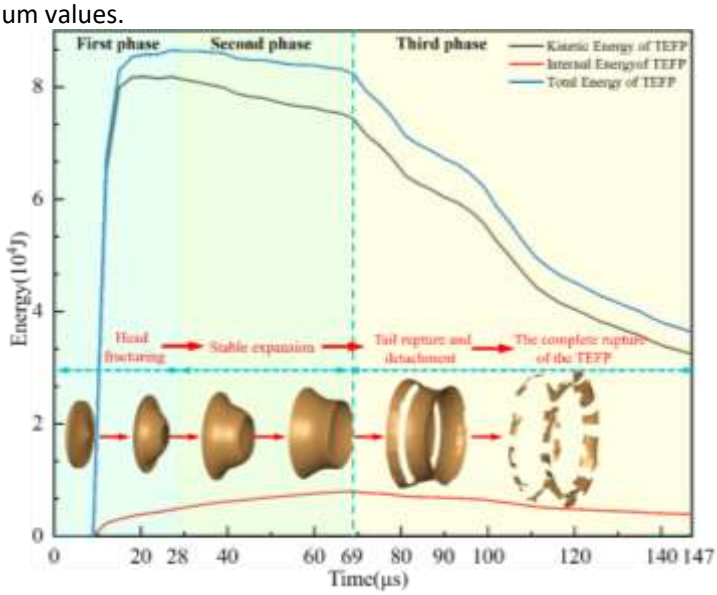

Figure 10 *Energy changes during the TEFP motion*

5.2 TEFP penetration mechanisms

Figure 11 illustrates the penetration processes that occurred when the TEFP impacted Q235 steel plates at different *h* values. The simulation results indicated that the TEFP achieved perforation of the target plate when $h \leq 110$ mm. When $h = 120$ mm, the TEFP achieved critical perforation of the target plate. When $h = 170$ mm and $h = 230$ mm, the TEFP was unable to perforate the target plate. In addition, when $h \leq 90$ mm, the TEFP tail did not rupture before the target plate was penetrated, and the TEFP was in its stable expansion phase when penetration began. When $h \geq 100$ mm, the TEFP

tail had already ruptured before the target plate was penetrated, and the TEFP was in its rupture and fragmentation phase when penetration began. When $h \geq 120$ mm, the TEFP tail had completely ruptured and detached from the main body by the time penetration had begun.

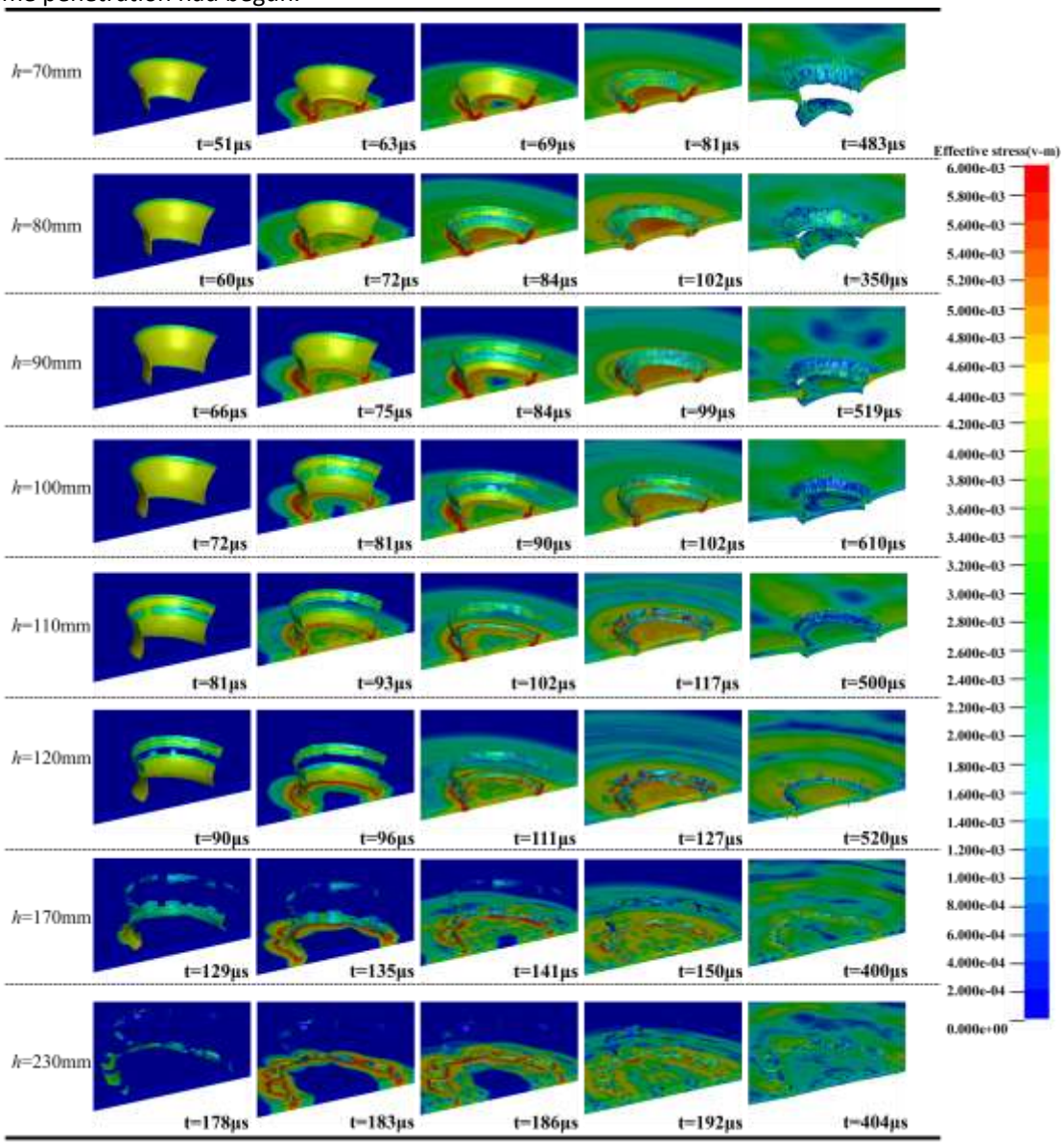

Figure 11 *TEFP penetration of Q235 steel targets at different h values*

Figure 12(a) compares the maximum TEFP diameter (d_m) at the beginning of penetration with the penetration-hole diameter (d_h) produced when target plates were perforated at different h values. Figure 12(b) presents the total and kinetic energies of the TEFP at the beginning of penetration for different h values. It is evident that, as h increased, the total and kinetic energies decreased, while d_h increased. Furthermore, at the beginning of penetration, d_m was smaller than d_h. The previously described TEFP formation process revealed that the TEFP possessed a significant radial velocity, and that as h increased, the TEFP diameter gradually increased. This diameter increase produced increases in d_h as h increased, and it led to a situation in which $d_h > d_m$. By referring to Figure 11, the process by which the TEFP perforated the target plate could be roughly divided into three phases, as is illustrated in Figure 13.

The first phase was the pit-opening phase of the target plate, during which the TEFP head initially penetrated the target plate. During this phase, the high velocity of the TEFP head generated a significant impact pressure at the collision site, which resulted in localized damage to the target plate and the rapid formation of a plastic deformation zone in its vicinity. In addition, due to the strong impact force exerted by the TEFP, the metal at the projectile–target contact point complied with the minimum-pressure criterion by primarily flowing in the direction opposite to that of the TEFP motion, thereby causing flanging around the penetration hole in the target plate. This phase had a very short duration.

The second phase was plastic hole expansion, during which significant plastic deformation and the formation of shear bands occurred in the penetration zone of the target plate. Additionally, the significant axial and radial velocities of the TEFP caused various portions of the target plate to be subjected to axial and radial compressive forces. These forces resulted in axial and radial displacements at these points, which led to the formation of a bulge on the back side of the target plate and an increase in the penetration-hole diameter. Simultaneously, during the compression process, mutual erosion of the TEFP and the target plate led to gradual reductions in the mass of the TEFP and in the thickness of the penetration zone of the target plate. High temperatures and pressures were generated during the TEFP penetration process, and these extreme conditions significantly reduced the strength of the target plate. This strength reduction produced substantial decreases in the shear resistance in the thickness direction of the target plate. Consequently, local stresses within the target plate exceeded the limits of the plate material, thereby causing cracks to form on the back side of the target plate by the end of the phase.

The third phase was the shear block formation phase. During this phase, the TEFP continued to penetrate the target plate, and the cracks on the back side of the target plate continuously expanded and propagated inward. When the TEFP began to penetrate the target plate with its tail still attached (h < 120 mm), the energy at the beginning of penetration was substantial. This energy was sufficient for the TEFP to overcome the fracture toughness of the material and initiate crack propagation. Ultimately, due to the residual kinetic energy of the TEFP and the inward propagation of the cracks, the projectile–target interaction zone was completely sheared off and expelled from the target plate, thereby forming a shear block with a certain velocity. Simultaneously, the frictional and shear forces caused the metal around the circular hole on the back side of the target plate to move in the same direction as the shear block; this motion resulted in flanging on the back side of the target plate. When the TEFP had a completely ruptured and detached tail as it began to penetrate the target plate (h ≥ 120 mm), crack formation was also possible on the back side of the target plate; these cracks could then propagate inward at certain h values. However, due to the low energy with which the TEFP initially penetrated the target plate and the limited kinetic energy that remained during this phase, the crack propagation ultimately ceased; thus, the target plate did not form a shear block.

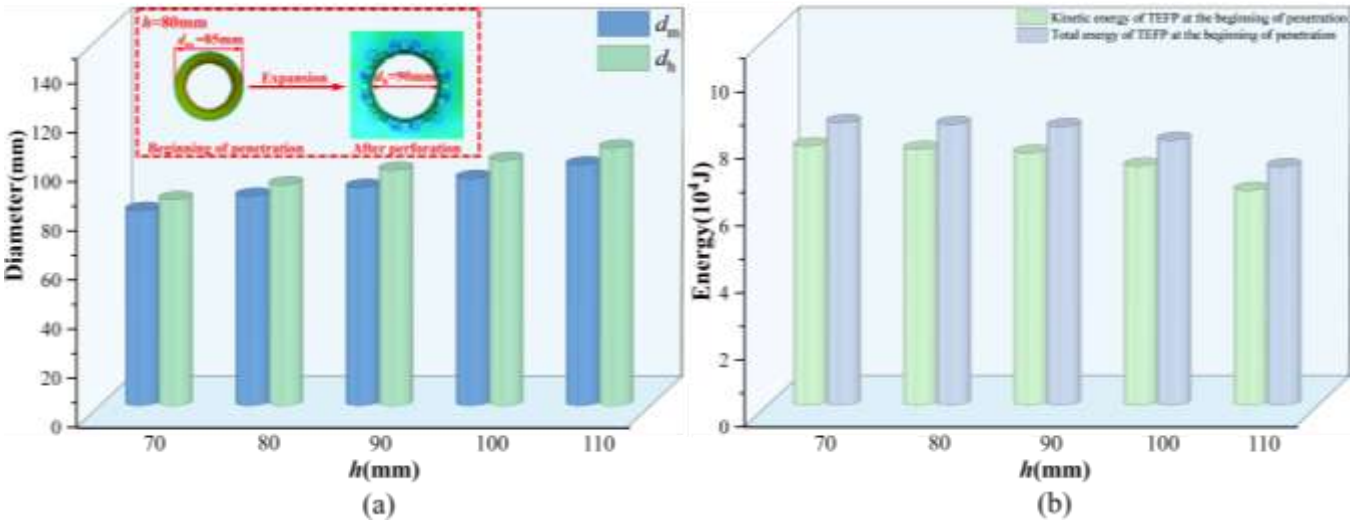

Figure 12 *(a) Comparisons between the d_m and d_h at different h values (b) the total and kinetic energies of the TEFP at the beginning of penetration*

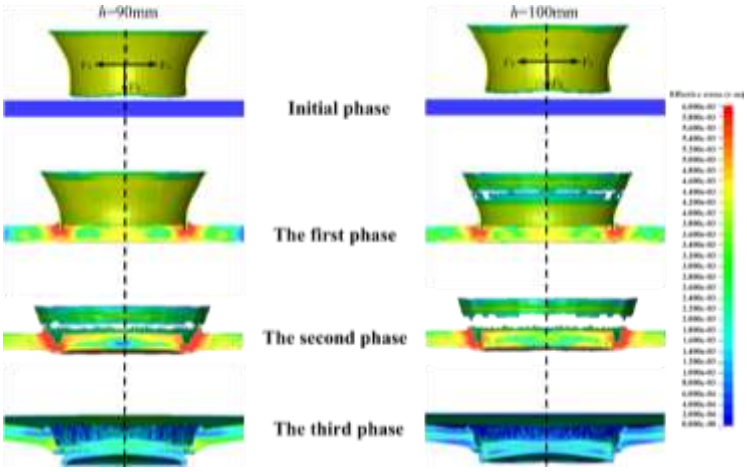

Figure 13 *Schematic diagram of the three stages of TEFP penetration*

Figure 14 presents energy–time curves for the perforation of steel plates by the TEFP at various *h* values. It is evident that both the kinetic and total energies of the TEFP first increased sharply, then gradually decreased, and eventually dropped sharply. The internal energy, however, exhibited a parabolic shape in that it rose and then fell. This process corresponds to that in which the TEFP was driven by the energy generated from the charge detonation and subsequently impacted the steel plate. The energy of the TEFP was completely consumed within approximately 34 μs during the perforation of the target plate. The kinetic energy of the target plate first increased sharply and then gradually decreased; this result was attributed to the substantial impact load exerted by the TEFP at the beginning of the penetration process. This impact load caused a sharp rise in the kinetic energy of the target plate, followed by a decline due to the erosion that occurred during penetration and the conversion of a significant portion of the TEFP energy into internal energy of the target plate. The total and internal energies of the target plate exhibited similar trends; both rose sharply initially and then stabilized. Furthermore, the increase in the internal energy of the steel plate was significantly greater than that of the kinetic energy; this result led to the conclusion that the majority of the energy imparted by the TEFP when it impacted the steel plate was converted into internal energy of the steel plate.

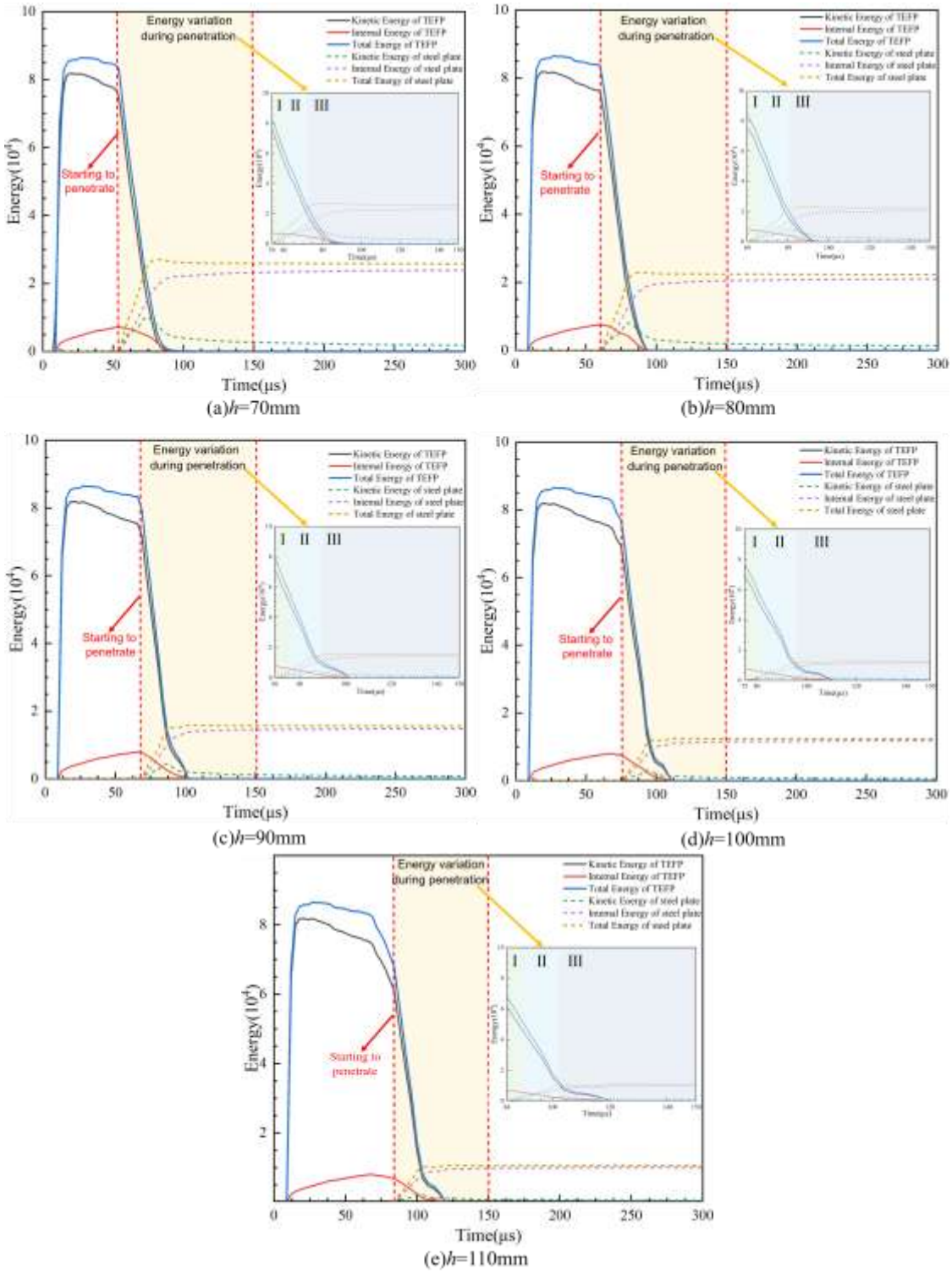

Figure 14 *Energy–time curves during perforation of steel plates by the TEFP*

Figure 15 depicts the kinetic energy consumption ratio during the three phases of the TEFP perforation process. The figure shows that the TEFP consumed the most kinetic energy during the plastic hole expansion phase, while it consumed the least kinetic energy during the shear-block formation phase. At different *h* values, the average amounts of kinetic energy consumed by the TEFP during the pit-opening phase, the plastic hole expansion phase, and the shear-block formation phase accounted for 26.0, 56.8, and 17.2% of the total kinetic energy, respectively. When *h* = 70 mm, the kinetic energy consumption ratio of the TEFP was greatest during the pit-opening phase (28.9%) and the shear-block formation phase (25.6%). When *h* = 100 mm, the kinetic energy consumption ratio reached its maximum value of 60.4% during the plastic hole expansion phase.

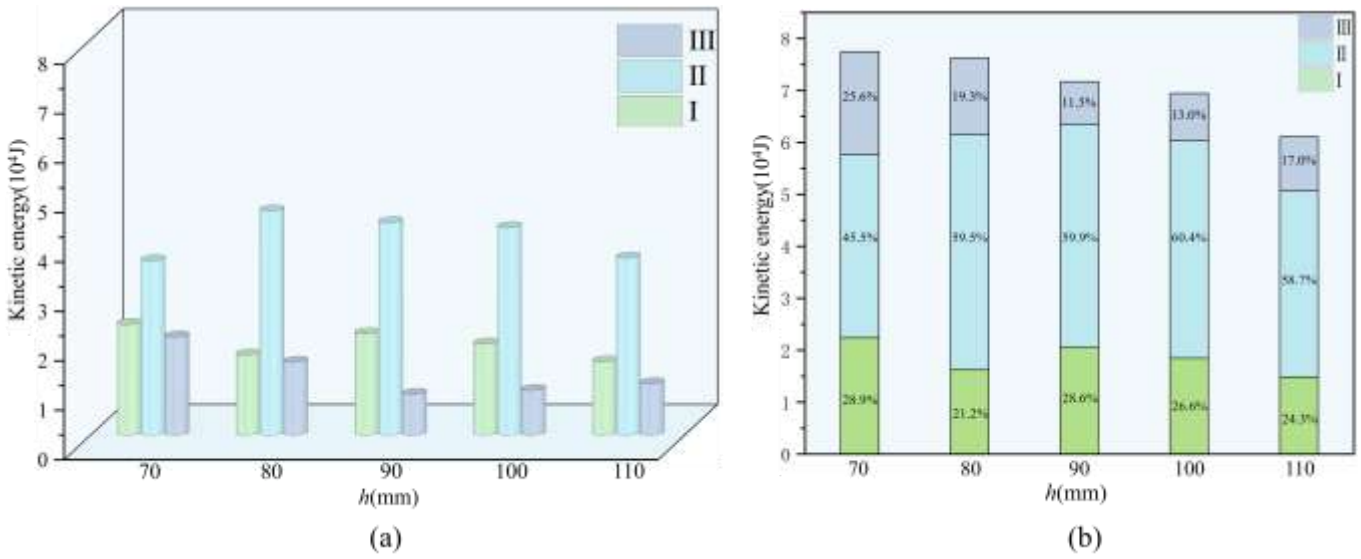

Figure 15 *(a) Change in kinetic energy of TEFP during three perforating phases (b) Kinetic energy ratio of the TEFP during the three perforation phases*

5.3 Optimum stand-off distance

Figure 16 compares the results of the penetration of target plates by the TEFP at different *h* values. It is evident that, when the tail of the TEFP had completely ruptured and detached from the main body, the TEFP did not perforate the target plate. Therefore, the optimal stand-off distance (h_o) for this TEFP structure was less than 120 mm. Additionally, when h < 120 mm, the mass of the shear block, diameter of the shear block, and d_h all gradually increased as h increased.

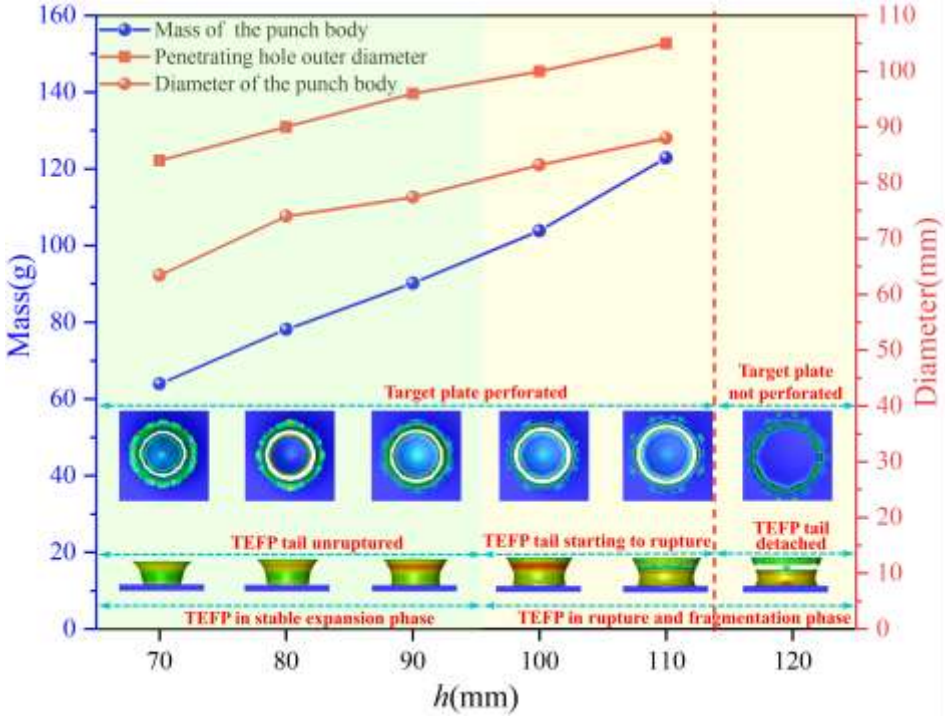

Figure 16 *Comparison of the results of the TEFP penetration of target plates at different h values*

To further investigate h_o, a parameter Ω was defined according to Equation (13):

$$\Omega = h_p d_p d_t \tag{13}$$

Where

$$\begin{cases} h_{\mathrm{p}} = h / D \\ d_{\mathrm{p}} = d_{\mathrm{h}} / d_{\mathrm{m}} \\ d_{\mathrm{t}} = d_{\mathrm{h}} / D \end{cases} \tag{14}$$

In Equations (13) and (14), h is the stand-off distance, D is the charge diameter, d_{h} is the penetration-hole diameter, and d_{m} is the maximum diameter of the TEFP at the beginning of penetration. The value of h_{p} reflects the TEFP penetration distance, the value of d_{p} reflects the reaming capability of the TEFP during penetration, the value of d_{t} reflects the ultimate reaming capability of the TEFP, and Ω reflects the comprehensive penetration and reaming capability of the TEFP.

Figure 17 compares the penetration and reaming capabilities of the TEFP at different h values. The figure shows that, for five different h values, d_{p} varied only slightly. In addition, h_{p}, d_{t}, and Ω reached their maximum values when h = 110 mm. Consequently, when h = 110 mm, the TEFP produced the penetration hole with the largest diameter and achieved its greatest flight distance. These results indicate that the best comprehensive penetration and reaming performance was achieved at this stand-off distance. Therefore, the optimal stand-off distance for this TEFP structure was 110 mm (1.96D). When h_{o} = 1.96D, the penetration-hole diameter of the target plate was 1.875D.

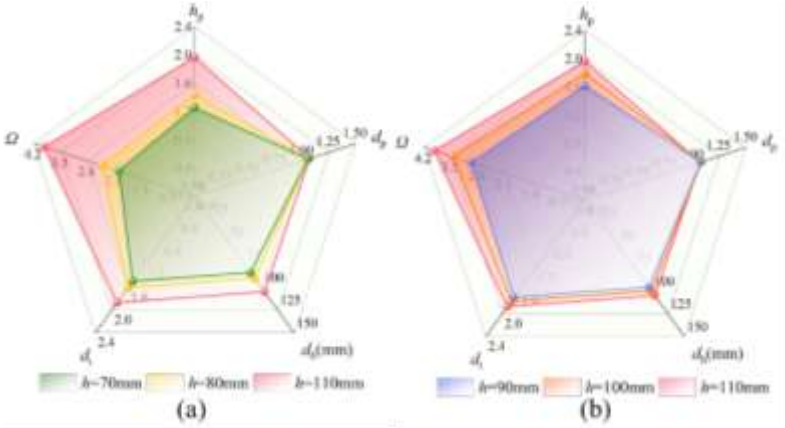

Figure 17 *Comparison of the TEFP penetration and reaming capabilities at different h values*

4. Conclusions

In this study, a series of penetration performance experiments were conducted for a TEFP with a charge diameter of 56 mm. This TEFP was used to penetrate Q235 steel plates at a variety of stand-off distances (h). Furthermore, numerical simulations were utilized to investigate the formation and penetration mechanisms of the TEFP, as well as to assess the effects of h on the penetration performance efficiency of the TEFP. The study produced five primary conclusions as follows.

1. Under the experimental conditions in this paper, the TEFP can penetrate the target plate at specific h values. However, as h increases, the TEFP begins to rupture, resulting in an inability to perforate the target plate. A microscopic analysis indicated that at specific h values, the grains in the steel plate experienced intense impacts, which caused refinement and recrystallization of the grains near the wall of the penetration hole. As h increases further, the grains in the steel plate do not experience refinement or recrystallization, and the target plate undergoes a relatively weak impact.
2. The TEFP formation process was divided into three phases: opening, stable expansion, and rupture and fragmentation. Throughout these phases, the TEFP diameter consistently increased. During the opening phase, an opening was formed in the head of the TEFP. During the stable expansion phase, the TEFP achieved a stable form without rupture, which resulted in a well-formed structure. During the rupture and fragmentation phase, the TEFP experienced sequential radial and axial ruptures; then it eventually formed radially distributed fragments. During the opening phase, the kinetic energy of the TEFP reached its maximum value of 8.128 kJ. Subsequently, the kinetic energy of the TEFP gradually decreased. During the stable expansion phase, the kinetic energy decreased from its maximum value by 8.5% due to kinetic energy consumption by the TEFP. From the beginning of the rupture and fragmentation phase to the formation of radially distributed fragments, the TEFP kinetic energy consumption caused the total remaining kinetic energy to decrease to 51.6% of its maximum value.

3. As h increased, the penetration kinetic energy of the TEFP gradually decreased and d_h increased. When h < 120 mm, the TEFP began to penetrate the target plate with its tail still attached. Under these conditions, the TEFP was capable of perforating the target plate, and $d_h > d_m$. The perforation of a Q235 steel plate by the TEFP could also be roughly divided into three phases: pit-opening, plastic hole expansion, and shear block formation. The largest amount of kinetic energy was consumed during the plastic hole expansion phase (56.8%), less was consumed during the pit-opening phase (26.0%), and the smallest amount was consumed during the shear-block formation phase (17.2%).
4. A method for assessing the penetration and reaming performance of the TEFP was established during this study. It was used to determine the optimal detonation stand-off distance, $h_o = 1.96D$, which resulted in a penetration-hole diameter of $1.875D$.

Acknowledgments

This research was supported by the National Natural Science Foundation of China, Grant Nos. 12202497. The authors would like to gratefully acknowledge this support.

Author's Contribuitions: Writing-original draft, Weijian Tang; **Test technical support,** Chong Ji, Yuting Wang, Xin Wang; **Writing-review & editing,** Changxiao Zhao, Huanyu Qian; **Numerical simulation technical support,** Yution Wang

Editor: Marcílio Alves

References

Lee H W.(2002) Oil well perforator design using 2D Eulerian code. International Journal of Impact Engineering 27(5):535-559.

Hu F, Wu H, Fang Q, et al.(2017) Impact performance of explosively formed projectile (EFP) into concrete targets. International Journal of Impact Engineering 109:150-166.

Liu JF, Long Y, Ji C, et al.(2018) Influence of layer number and air gap on the ballistic performance of multi-layered targets subjected to high velocity impact by copper EFP. International Journal of Impact Engineering 112:52-65.

Guo H, Zheng Y, Yu Q, et al.(2018) Penetration behavior of reactive liner shaped charge jet impacting thick steel plates. International Journal of Impact Engineering 126:76-84.

Dehestani P, Fathi A, Daniali M H.(2019) Numerical study of the stand-off distance and liner thickness effect on the penetration depth efficiency of shaped charge process. Journal of Mechanical Engineering Science 233(3):977-986.

Wang C, Xu W, Yuen K C S.(2018) Penetration of shaped charge into layered and spaced concrete targets. International Journal of Impact Engineering 112:193-206.

Fu J, Chen Z, Hou X, et al.(2013) Simulation and Experimental Investigation of Jetting Penetrator Charge at Large Stand-off Distance. Defence Technology 9(2):91-97.

Chen C, Wang X M, Li W B, et al.(2015) Effect of matching of detonation waveform with liner configuration on the rod-like jet formation. Explosion and Shock Waves 35(06):812-819. (in Chinese).

Liu JF, Long Y, Ji C, et al.(2015) The influence of liner material on the dynamic response of the finite steel target subjected to high velocity impact by explosively formed projectile. International Journal of Impact Engineering 109:264-275.

Cardoso D, Teixeira-Dias F.(2016) Modelling the formation of explosively formed projectiles (EFP). International Journal of Impact Engineering 93:116-127.

Han W, He Y, Shen X J, et al.(2019) Investigation of EFP Forming and Penetration of Ta /Zr Double-Layered Shaped Charge Liner. Journal of Ordnance Equipment Engineering 40(4):163-167. (in Chinese).

König PJ, Mostert FJ.(2001) The design and performance of annular EFP's. 19th International Symposium on Ballistics.

Chick M C, Bussell T C, Lam C P.(1998) Development of a cookie-cutter explosively formed projectile. 17th International Symposium on Ballistics.

Xu W, Wang C, Chen D.(2019) Formation of a bore-center annular shaped charge and its penetration into steel targets. International Journal of Impact Engineering 127:122-134.

Xu W, Wang C, Yuan J, et al.(2019) Bore-center annular shaped charges with different liner materials penetrating into steel targets. Defence Technology 15(5):796-801.

Meister J, Haller F.(2001) Experimental and numerical studies of annular projectile charges. 19th International Symposium on Ballistics.

Richard F, LaMar T, William N.(2010) Toroidal warhead development. 25th International Symposium on Ballistics.

Murr E L, Trillo A E, Pappu S, et al.(2002) Adiabatic shear bands and examples of their role in severe plastic deformation. Journal of Materials Science 37(16): 3337-3360.

Li W B, Wang X M, Li W B.(2009) The effect of annular multi-point initiation on the formation and penetration of an explosively formed penetrator. International Journal of Impact Engineering 37(4):414-424.

Shen Fei, Wang Hui, Yuan Jianfei.(2014) A simple method for determining parameters of JWL EOS. JOURNAL OF VIBRATION AND SHOCK 33(09):107-110.

R Qi, G S Langdon, T J Cloete, et al.(2020) Behaviour of a blast-driven ball bearing embedded in rear detonated cylindrical explosive. International Journal of Impact Engineering 146:103698.

Gao Y X, Ji C, Wang X, et al.(2024) Oblique penetration performance of Explosively Formed Projectile (EFP) on 6061 aluminum target: experiments and simulations. Latin American Journal of Solids and Structures 21(1):e515.

Johnson G R, Cook W H.(1985) Fracture characteristics of three metals subjected to various strains, strain rates, temperatures and pressures. Engineering fracture mechanics 21(1):31-48.

Mengtao Zhang, Yang Pei, Xin Yao, et al.(2023) Damage assessment of aircraft wing subjected to blast wave with finite element method and artificial neural network tool. Defence Technology 25(07):203-219.

Kennedy J E.(1972) Explosive output for driving metal. Proceeding of the 12th Annual Symposium of the New Mexico Section of the ASME 01-32.

Wang Z, Jiang J W, Wang S Y, et al.(2017) A calculation model of velocity of tandem EFP double layer liners. Acta Armamentarii 38(7):1301-1306. (in Chinese).

Chou P C, Flis W J, Forsyth C M.(1986) A simplified model of jet formation in hemispherical shaped charges. Proceedings of the 9th International Symposium on Ballistics 263-272

Chou P C, Flis W J, Forsyth C M.(1986) A simplified model of jet formation in hemispherical shaped charges. Proceedings of the 9th International Symposium on Ballistics 263-272